

Chapter 5

Relationships Between Seismic Wave-Speed, Density, and Electrical Conductivity Beneath Australia from Seismology, Mineralogy, and Laboratory-Based Conductivity Profiles

A. Khan, S. Koch, T.J. Shankland, A. Zunino and J.A.D. Connolly

Abstract We present maps of the three-dimensional density (ρ), electrical conductivity (σ), and shear-wave speed (V_S) structure of the mantle beneath Australia and surrounding ocean in the depth range of 100–800 km. These maps derived from stochastic inversion of seismic surface-wave dispersion data, thermodynamic modeling of mantle mineral phase equilibria, and laboratory-based conductivity models. Because composition and temperature act as fundamental parameters, we obtain naturally scaled maps of shear-wave speed, density, and electrical conductivity that depend only on composition, physical conditions (pressure and temperature), and laboratory measurements of the conductivity of anhydrous mantle minerals. The maps show that in the upper mantle ρ , σ and V_S follow the continental-tectonic division that separates the older central and western parts of Australia from the younger eastern part. The lithosphere beneath the central and western cratonic areas appears to be relatively cold and Fe-depleted, and this is reflected in fast shear-wave speeds, high densities, and low conductivities. In contrast, the lithosphere underneath younger regions is

Electronic supplementary material The online version of this chapter (doi:[10.1007/978-3-319-15627-9_5](https://doi.org/10.1007/978-3-319-15627-9_5)) contains supplementary material, which is available to authorized users.

A. Khan (✉) · S. Koch
Institute of Geophysics, ETH Zürich, Zürich, Switzerland
e-mail: amir.khan@erdw.ethz.ch

T.J. Shankland
Geophysics Group, Los Alamos National Laboratory, Los Alamos, USA

A. Zunino
Niels Bohr Institute, University of Copenhagen, Copenhagen, Denmark

J.A.D. Connolly
Institute of Geochemistry and Petrology, ETH Zürich, Zürich, Switzerland

relatively hot and enriched with Fe, which is manifested in slow shear-wave speeds, low densities, and high conductivities. This trend appears to continue to depths well below 300 km. The slow-fast shear-wave speed distribution found here is also observed in independent seismic tomographic models of the Australian region, whereas the coupled slow-fast shear-wave speed, low-high density, and high-low electrical conductivity distribution has not been observed previously. Toward the bottom of the upper mantle at 400 km depth marking the olivine \rightarrow wadsleyite transformation (the “410-km” seismic discontinuity), the correlation between V_S , ρ , and σ weakens. In the transition zone, V_S , ρ , and σ are much less correlated indicating a significant compositional contribution to lateral heterogeneity. In particular, in the lower transition zone, σ and ρ appear to be governed mostly by variations in $\text{Fe}/(\text{Fe} + \text{Mg})$, whereas lateral variations in V_S result from changes in $(\text{Mg} + \text{Fe})/\text{Si}$ and not, as observed in the upper mantle, from temperature variations. Lower mantle lateral variations in thermochemical parameters appear to smooth out, which suggests a generally homogeneous lower mantle in agreement with seismic tomographic images of the lower mantle. As a test of the regional surface-wave-based conductivity model, we computed magnetic fields of 24 h S_q variations and compared these to observations. The comparison shows that while our predicted conductivity model improves the fit to observations relative to a one-dimensional model, amplitudes of the computed conductivity anomalies appear not to be large enough to enable these to be discriminated at present.

Keywords Electrical conductivity • Seismic wave-speed • Tomography • Phase equilibria • Surface waves • Electromagnetic sounding • Mantle composition • Mantle temperatures

5.1 Introduction

Large-scale features of elastic properties from seismic tomography are reasonably well resolved and show strong correlation with surface-tectonic features (e.g., Schaeffer and Lebedev 2015; Lekic and Romanowicz 2012; Rawlinson et al. 2015), but smaller scale variations appear to be less well resolved and to have more complex thermal and chemical origins (e.g., Trampert and van der Hilst 2005). Mantle convection simulations favor a heterogeneous mantle made of a mechanical mixture of basalt and harzburgite (e.g. Christensen and Hofmann 1994; Xie and Tackley 2004), which are the products of partial melting at mid-ocean ridges. While such models produce a natural metric for understanding the generation and continued renewal of a laterally heterogeneous mantle through subduction of differentiated oceanic lithosphere (e.g., Xu et al. 2008), it is not yet clear whether such mixture models can account for the complexity observed across a wide range of geophysical data (e.g., Helffrich and Wood 2001; Schmerr 2015; Kawai and Tsuchiya 2015).

Detailed maps of compressional and shear-wave velocity models exist, but there are fewer constraints on mantle density structure (e.g., Kennett 1998; Ishii and Tromp 2004) because seismic data underlying tomographic models are relatively insensitive to density (e.g., Resovsky and Ritzwoller 1999; Romanowicz 2001; Kuo and Romanowicz 2002). Yet, geodynamical modeling expresses internal dynamics driven by lateral density variations (e.g., Forte and Perry 2000; Deschamps et al. 2001), and improved knowledge of mantle density structure could prove an important additional constraint.

Complementary means to obtain structural information can come from studies that relate elastic properties to chemical composition and crystal structure to constrain systematic relations between seismic wave-speed and density in mantle minerals (e.g., Birch 1961; Shankland 1972). These systematics can subsequently be compared to density, P-, and S-wave speed profiles that are deduced from geophysical studies or even be applied in an inverse sense to obtain compositional information (e.g., Shankland 1977). Other means rely on transport properties, e.g., electrical and thermal conductivities, and viscosity, (e.g., Shankland 1981; Poirier 2000). Electrical conductivity, for example, is more sensitive to composition and temperature than in elasticity (e.g., Xu et al. 2000; Dobson and Brodholt 2000; Khan et al. 2006; Verhoeven et al. 2009). However, the perceived advantage of studies based on electrical conductivity is diminished by a smaller number of world-wide geomagnetic observatories in comparison with the present-day global network of seismic stations (e.g., Kuvshinov 2012).

Global and semi-global three-dimensional (3D) conductivity images of the mantle are most reliable in imaging transition zone and outermost lower mantle (e.g., Utada et al. 2009; Kelbert et al. 2009; Tarits and Mandea 2010; Shimizu et al. 2010; Semenov and Kuvshinov 2012), where they show relatively low lateral and radial resolution in comparison with their seismic counterparts. Resolution aside, current global-scale conductivity, and seismic tomography maps appear to have few features in common (for a comparison see, e.g., Semenov and Kuvshinov 2012). Fast and slow velocity anomalies that are usually interpreted as evidence of cold and hot mantle conditions, respectively, do not always correlate with low and high conductivities as might be expected from the observation that conductivity has a strong temperature dependence following an Arrhenius relation (e.g., Poirier 2000). On a more fundamental level, transport and elastic properties of minerals are different phenomena and per se need not be correlated. However, if temperature is the dominant source of mantle velocity anomalies as frequently argued (e.g., Goes et al. 2000), then we might expect a minimum degree of correlation. Such a correlation is not usually observed for reasons yet to be determined. On the other hand, if composition in the form of variations in major element chemistry is responsible for a significant part of the signal, then we might not observe significant correlations between the two physical properties. Hence, these features could provide potential means to unravel compositional contributions to lateral variations in mantle properties.

To examine relations between elastic properties and electrical conductivity, we link elasticity, density, and electrical conductivity through thermodynamic modeling of mantle minerals (e.g., Khan et al. 2006; Verhoeven et al. 2009). Using a

self-consistent scheme (Gibbs free-energy minimization) to calculate phase equilibria, followed by equation of state modeling, we compute properties that depend only on physical conditions (pressure and temperature) and on chemical composition (e.g., Connolly 2005; Ricard et al. 2005; Stixrude and Lithgow-Bertelloni 2005; Piazzoni et al. 2007). Thus, the use of free-energy minimization methods results in physically realistic models that include natural scaling between the various properties.

We first consider shear-wave velocities of the mantle beneath continental Australia to a depth of 800 km that are derived from stochastic inversion of surface-wave dispersion data as described in Khan et al. (2013). In the inversion, we map mantle temperatures and compositions from elastic responses. Having these properties together with independent laboratory conductivity measurements of different mineralogies and temperatures permit calculating mantle electrical conductivities independently of elastic properties at depth. From these conductivity maps, it is possible to calculate an equivalent conductivity response. Hence, this approach provides a natural basis for analyzing different data sets and for addressing fundamental issues related to the structure and constitution of the Earth (e.g., Khan et al. 2006, 2013; Verhoeven et al. 2009; Fullea et al. 2009, 2011, 2012; Afonso et al. 2013a, b; Jones et al. 2013; Drilleau et al. 2013; Kuskov et al. 2014).

Joint inversion of seismic, gravity, and electromagnetic sounding data would be a preferable approach; owing to the complexity and the computational resources required for solving the joint problem, it is beyond the scope of this study and will be considered in future studies. However, we would like to emphasize that this procedure, while based on inversion of seismic data, does not imply that the derived conductivity structure simply or tautologically follows that dictated by seismic data because independent chemical, mineralogical, and laboratory conductivity databases are interposed. Finally, we note that because the main purpose of this study is to examine relative behaviors of elastic and transport properties, we do not consider the inverse problem of constraining composition and temperature from seismic data per se in any detail here, but consider this part a *fait accompli* with details supplied in the previous treatment (Khan et al. 2013).

As the main focus in this study centers on mantle compositional (major elements) and thermal variations, we assume anhydrous and subsolidus conditions, i.e., we consider the mantle to be dry and melt-free. We make such a simplifying assumption out of necessity as (1) thermodynamic data for modeling shear-wave speed for water- and melt-bearing phases are uncertain and (2) several studies have showed that an anhydrous mantle is not inconsistent with conductivity profiles obtained from global electromagnetic sounding data (e.g., Manthilake et al. 2009; Khan and Shankland 2012). Moreover, although available data have been used to construct parameterized approaches to modeling the effect of water and melt on shear-wave speed and conductivity (e.g., Laske et al. 2011; Goes et al. 2012), these cannot be modeled self-consistently in line with the main approach of this study. It is left to future studies to consider this and contributions arising from other effects such as the presence of melt (e.g., Shankland et al. 1981; Park and Ducea 2003; Toffelmier and Tyburczy 2007; Khan and Shankland 2012; Koyama et al. 2006, 2013; Karato 2011; Pommier 2014).

5.2 Data and Methods

5.2.1 The Forward Problem

The solution to the forward problem, i.e., estimation of surface-wave dispersion data (d_{seis}) and magnetic field variations (d_{mag}) from composition c , temperature T , and a laboratory conductivity database (d_{σ}) can be summarized as follows:

$$\begin{array}{ccccc}
 c, T & \xrightarrow{g_1} & M & \xrightarrow{g_2} & \rho, V_S, V_P & \xrightarrow{g_4} & d_{\text{seis}} \\
 & & & \searrow^{g_3} & & & \\
 & & & & d_{\sigma} & \xrightarrow{g_5} & \sigma & \xrightarrow{g_5} & d_{\text{mag}}
 \end{array}$$

where M indicates equilibrium modal mineralogy (all parameters are implicitly assumed to be functions of radius) and the various g 's embody physical laws in the form of thermodynamic modeling (g_1), equation of state modeling (g_2), bulk rock conductivity estimation (g_3), surface-wave dispersion calculations (g_4), and computation of magnetic field variations (g_5). Here, we do not consider the part related to g_4 for reasons outlined earlier. From the above forward scheme, we observe that electrical conductivity is not immediately available from free-energy minimization, but has to be computed using separate laboratory-based conductivity data.

5.2.2 Parameterization

As outlined in more detail in Khan et al. (2013), we parameterized the model laterally in terms of $5^\circ \times 5^\circ$ pixels and beneath the center of each pixel radially by a number of layers with a fixed node-spacing in the mantle of 50–200 km for temperature and composition (Fig. 5.1). The crust is parameterized using purely physical properties that include P- and S-wave speeds, density, conductivity, and depth to crust-mantle interface. With these parameters assigned, we performed Gibbs free-energy minimization (to be described below) and computed modal mineralogy and mantle physical properties on a denser fixed radial grid with node spacing in the range of 10–50 km.

5.2.3 Thermodynamic Modeling

Application of free-energy minimization methods in geophysics is not new (e.g., Saxena and Eriksson 1983; Wood and Holloway 1984; Kuskov and Panferov 1991; Sobolev and Babeyko 1994; Bina 1998; Fabrichnaya 1999), but it has been limited by the extent of early thermodynamic databases. Here, we use the

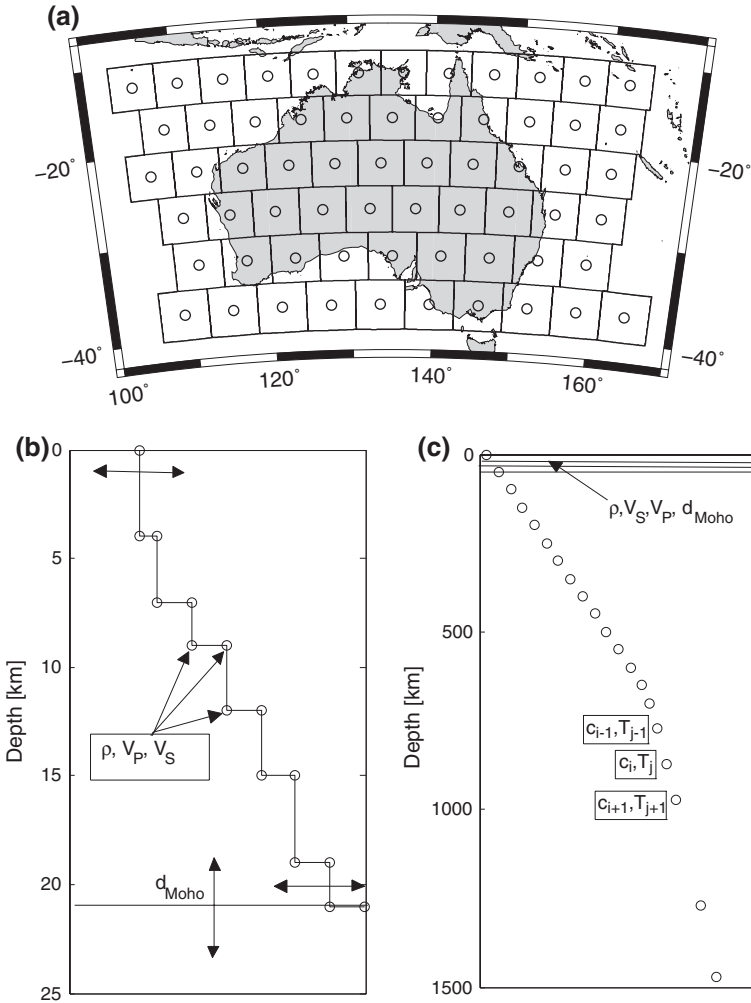


Fig. 5.1 Model parameterization: lateral grid spacing is $5^\circ \times 5^\circ$ (a) and radially model parameterization consists of layers (b–c). The crust (b) is delineated by density (ρ), P- and S-wave speeds (V_P , V_S), and depth to crust-mantle interface (d_{Moho}). Mantle layers (c) are parameterized by composition (C) and temperature (T). Circles in both plots denote location of a set of prefixed depth nodes (corresponding to indices i and j in plot c), except in the crust where depth to crust-mantle interface is variable. Modified from Khan et al. (2013)

free-energy minimization strategy described by Connolly (2009) to predict rock mineralogy, elastic moduli, and density as a function of pressure, temperature, and bulk composition. For this purpose, we employ the thermodynamic formulation of Stixrude and Lithgow-Bertelloni (2005) with parameters as in Stixrude and Lithgow-Bertelloni (2011). Possible mantle compositions are explored within the $\text{Na}_2\text{O}-\text{CaO}-\text{FeO}-\text{MgO}-\text{Al}_2\text{O}_3-\text{SiO}_2$ (NCFMAS) system, which accounts

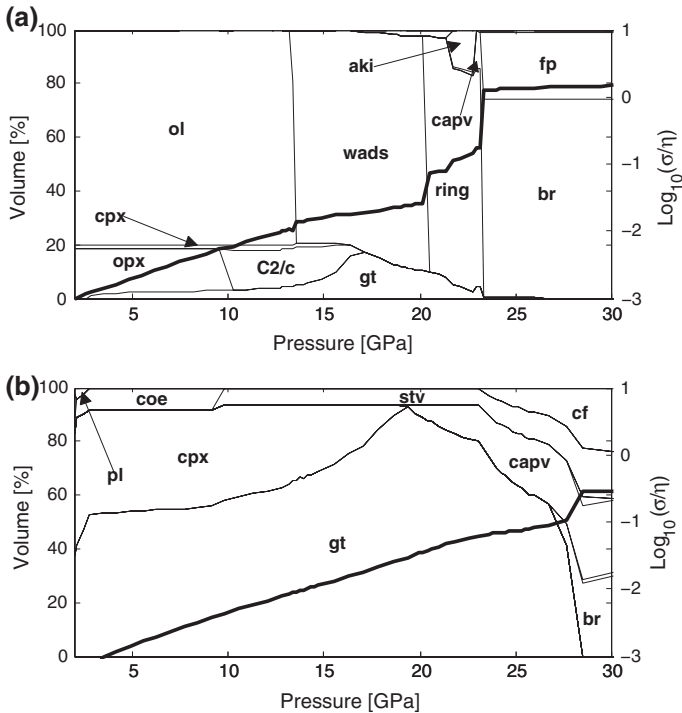


Fig. 5.2 Variations in phase proportions and physical properties in the upper mantle, transition zone, and outermost lower mantle (0–30 GPa, 0–750 km depth). Aggregate rock conductivity (*bold black lines*) and phase equilibria are calculated for two different mantle compositions in the NCFMAS system (comprising oxides of the elements Na_2O – CaO – FeO – MgO – Al_2O_3 – SiO_2): harzburgite (a) and MORB (b) along the mantle adiabat of Brown and Shankland (1981) (see Fig. 5.3). Phases are: olivine (ol), orthopyroxene (opx), clinopyroxene (cpx), pl (plagioclase), coe (coesite), stishovite (stv), high-pressure Mg-rich cpx (C2/c), garnet (gt), wadsleyite (wad), ringwoodite (ring), akimotoite (aki), calcium silicate perovskite (capv), ferropericlase (fp), bridgemanite (br), and calcium ferrite (cf)

for ~99 % of the mass of Earth’s mantle (e.g., Irifune 1994). Because the equilibrium assumption is dubious at low temperature (e.g., Wood and Holloway 1984), for models that require rock properties at temperatures below 800 K, the stable mineralogy is first calculated at 800 K and its physical properties are then computed at the temperature of interest. Bulk rock elastic moduli are estimated by Voigt-Reuss-Hill (VRH) averaging. The pressure profile is obtained by integrating the load from the surface (boundary condition $p = 10^5$ Pa). Examples of equilibrium mineralogy and bulk rock conductivity for two different compositions along the mantle adiabat of Brown and Shankland (1981) are shown in Fig. 5.2. The influence of phase equilibria in these examples representing end-member compositions is apparent from the discontinuities in conductivity associated with mineral phase transformations. The difference in geophysical response incurred by the two

conductivity profiles shown in Fig. 5.2 is easily detectable with an appropriate set of electromagnetic response functions.

Uncertainties associated with the thermodynamic data are notoriously difficult to assess because of the nonlinearity of the free-energy minimization problem and correlations among the various thermodynamic parameters. A preliminary Monte Carlo analysis of this uncertainty indicates uncertainties in density, P-, and S-wave speeds on the order of <0.1, <0.5, and <1 %, respectively (unpublished data). Alternative means of investigating this uncertainty are illustrated in the applications of Afonso et al. (2013a) and Kuskov et al. (2014) that employ similar approaches to the method outlined here. In a methodological study of determining thermo-chemical mantle structure from a diverse set of geophysical data, Afonso et al. (2013a) assess the uncertainty by comparing predicted and observed modal compositions for a set of xenoliths and generally find that differences between computed and observed values are within experimental error. Differences in physical properties between computed and laboratory measurements are also found to be negligible. In a related study, Kuskov et al. (2014) map the thermo-chemical structure of the lithospheric mantle beneath the Siberian craton using seismic velocity profiles and find that temperatures and depth to the lithosphere–asthenosphere boundary can only be determined to within an accuracy of ± 100 °C and ± 30 km, respectively, given the uncertainties in the thermodynamic parameters and modeled velocities.

5.2.4 Laboratory Electrical Conductivity Data

The conductivity data employed in this study are detailed in Khan and Shankland (2012) and shown in Fig. 5.3. The conductivity database comprises the minerals olivine (ol), orthopyroxene (opx), clinopyroxene (cpx), garnet (gt), wadsleyite (wads), ringwoodite (ring), ferropiclasite (fp), and bridgemanite (br). This data set allows us to model mineral conductivities as functions of major element composition, temperature, and pressure. In order to construct a bulk conductivity profile from single mineral conductivities, we make use of a self-consistent solution based on effective medium theory (Landauer 1952; Berryman 1995) for conducting composites (for more discussion see, e.g., Xu et al. 2000; Khan and Shankland 2012)

$$\sum_{i=1}^N x_i \left[\frac{\sigma_i - \sigma_{sc}}{\sigma_i + 2\sigma_{sc}} \right] = 0, \quad (5.1)$$

where x_i is volume fraction of mineral i , N the total number of minerals, and σ_{sc} represents the self-consistent solution that has to be determined iteratively to satisfy Eq. 5.1, while bounded by the Hashin-Shtrikman bounds. The latter are the narrowest bounds that exist for a multiphase system in the absence of information about the geometrical arrangement of the constituent phases (Hashin and

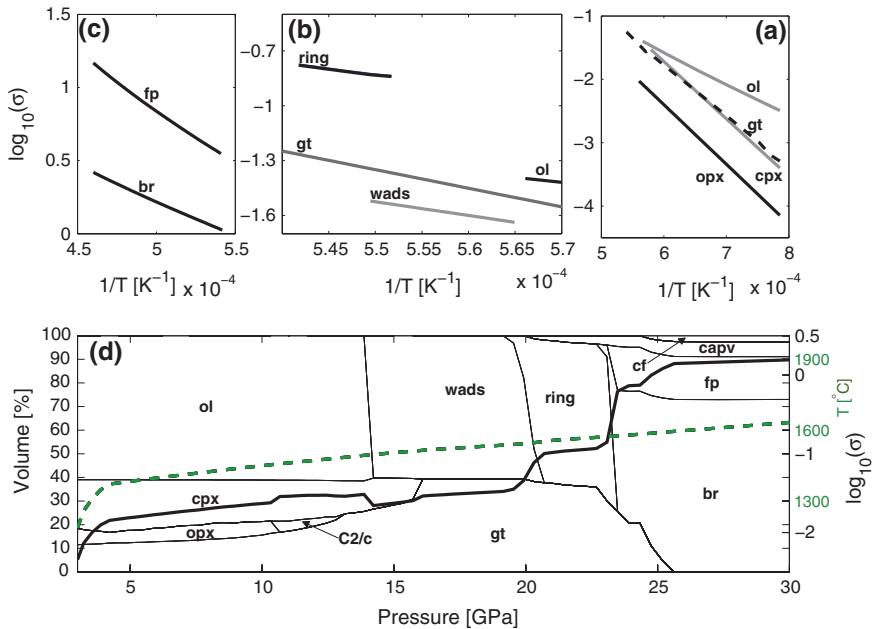


Fig. 5.3 Summary of mineral electrical conductivities measured in the laboratory as a function of inverse temperature for **a** upper mantle, **b** transition zone, and **c** upper part of lower mantle. **d** Variations in mineral phase proportions and laboratory-based bulk conductivity profile. For the example shown here bulk conductivity profile and mineral modes were computed using a homogeneous adiabatic pyrolytic and anhydrous mantle as a function of pressure (depth). The *solid black* and *dotted green* lines in plot **d** show bulk conductivity and the adiabat of Brown and Shankland (1981), respectively. For phase names, see Fig. 5.2; the main text contains further discussion. Modified from Khan et al. (2011)

Shtrikman 1962; Watt et al. 1976). Phases present at levels <10 vol% (e.g., coesite, stishovite, and akimotoite) are not considered as these have no effect on bulk conductivity (e.g., Khan et al. 2011).

To illustrate the methodology, we computed modal mineralogy and corresponding self-consistently determined bulk conductivity profile for a homogeneous adiabatic mantle made of pyrolite (Fig. 5.3). The bulk conductivity profile reveals a number of interesting features observed previously that include an almost vanishing “410-km” discontinuity (olivine → wadsleyite), and relatively strong “520-km” and “660-km” discontinuities (wadsleyite → ringwoodite and ringwoodite → bridgmanite + ferriperovskite), respectively. As a consequence, absence of a strong “410” discontinuity in conductivity is likely to be a prominent feature of conductivity images relative to those showing shear-wave speed. Variations in V_S are expected to be strong across the “410.” In the case of the “660,” a relatively strong compositional dependence through variations in Fe content is possible.

5.3 Results and Discussion

Maps of mean mantle shear-wave speed [these are anelastically corrected using the approach outlined in Khan et al. (2013)], electrical conductivity, density, mineralogy, and thermochemical variations derived from inversion of surface-wave data are shown in Fig. 5.4. Mean bulk compositions are indicated as ratios of the three major elements Mg, Fe, and Si derived from the oxide models c ; the remaining elements are less well determined. The mean model was computed from the 10^4 models that were sampled and considered in the analysis of Khan et al. (2013). Note that variations are displayed relative to mean reference models that are computed from lateral averages of all sampled models across all pixels. The mean reference profiles are shown in Fig. 5.5. Moreover, 1D marginal posterior distributions for the parameters displayed in Fig. 5.4 (for a single location in central Australia) are depicted in Fig. 5.6. With regard to the mean model displayed here, we would like to note that any model picked randomly from the posterior probability distribution is as representative as the mean or median model, if not more so, since the latter models are unlikely to be sampled and therefore constitute a poor representation of the solution (small posterior probability).

Rather than compute uncertainty measures such as credible intervals from the suite of sampled models (see Khan et al. 2013), we depict model parameter uncertainty in the form of a movie sequence that displays 250 models taken randomly from the posterior distribution (see online supporting material). The movie provide insight into overall model variability. The features that are well resolved will tend to be more stable across the maps and models, whereas less well-resolved features appear more unstable. Variations in mantle temperature and physical properties, for example, are seen to be remarkably stable, particularly throughout the upper mantle. Compositional variations, on the other hand, only appear to be stable down to 200 km depth. However, a closer look actually reveals that the relative geographical distribution of compositional variations is stable. As an aid in interpreting the maps, we have computed correlations between the various physical and thermochemical parameters as a function of depth (Figs. 5.7 and 5.8). Note that correlations are shown as distributions that are computed from 10^4 models, i.e., from all samples considered in Khan et al. (2013), and indicate the probability for observing a correlation coefficient in a particular range. The more peaked the correlation coefficient is, the better the parameter is resolved. It must also be mentioned that the correlations in and around the transition zone do not necessarily coincide with the depths at which mineralogical phase transitions occur.

5.3.1 Correlated Lateral Variations of Physical Properties

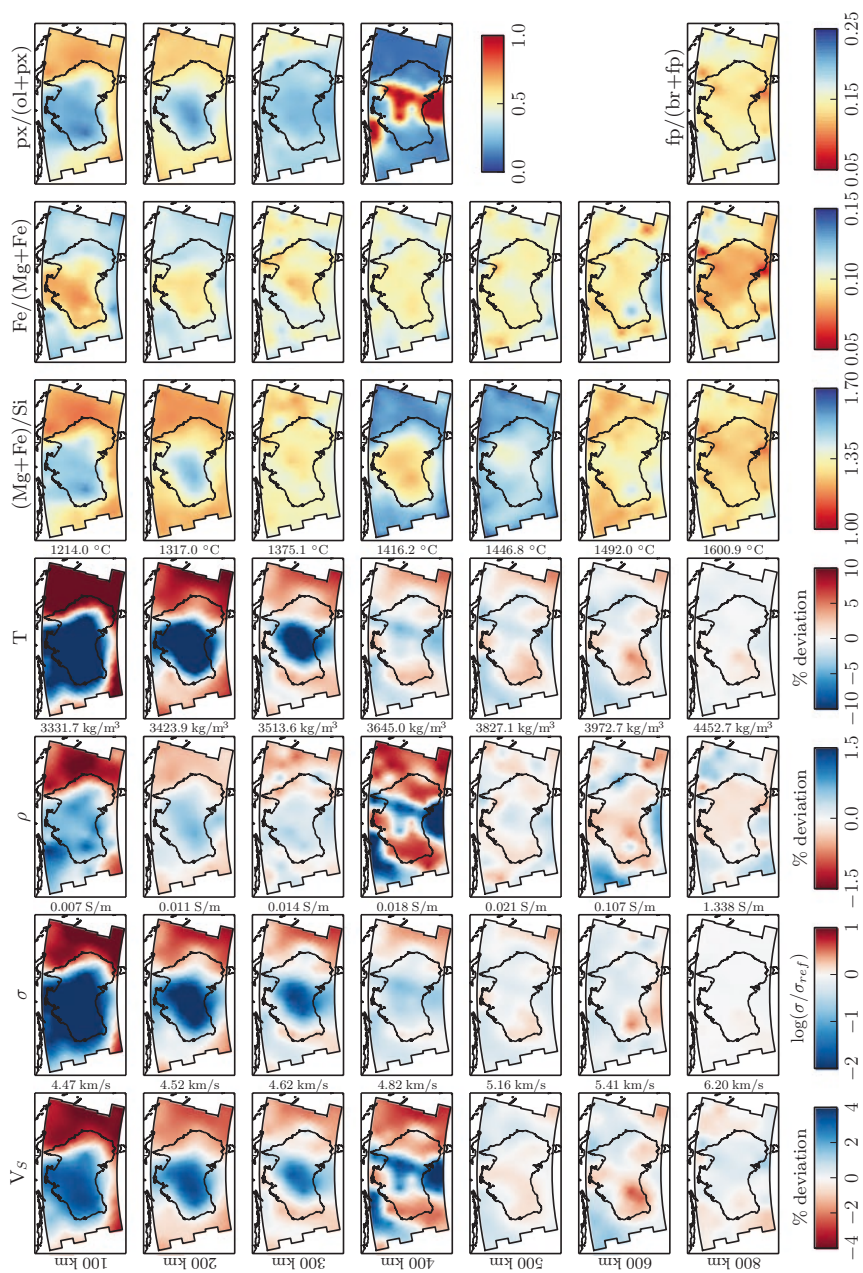
Figures 5.7 and 5.8 provide a number of interesting interrelationships as lateral correlations between physical properties, chemistry, mineralogy, and temperature.

The distributions indicate variations with lateral distances for various depth ranges indicated by color coding. Thus, lateral changes are isobaric, i.e., independent of phase changes with pressure. We emphasize the significance only of distributions outside the range -0.5 to 0.5 where statistics can be inconclusive. This section interprets physical connections between different variables, and the following section treats their geophysical variations.

The top row of Fig. 5.7 displays temperature effects and has the clearest correlations, either strongly positive or negative. As expected, density ρ decreases with T as a consequence of thermal expansion. Velocities also decrease with T as measured in laboratory measurements, a consequence of weakening interatomic bonds (Wang 1970). The positive conductivity variation with T reflects the exponential increase of σ with T in semiconductors and thus is a right-left mirror image of the other two figures. With increasing depth, lateral thermal effects become less correlated, produce fewer lateral changes of physical properties, and require other explanations.

In the second row, density increases with replacement of Mg by the heavier element Fe in crystal structures; within a given crystal structure, this replacement leads to decreased shear-wave speed (e.g., Birch 1961; Shankland 1972) as in Fig. 5.7e. Electrical conductivity within different silicate mineralogies commonly increases with Fe content (e.g., Hirsch et al. 1993; Yoshino et al. 2012), and this is seen in Fig. 5.7f.

In the third row, to the degree that increasing $(\text{Mg} + \text{Fe})/\text{Si}$ represents increase of ρ as olivine increases with respect to pyroxene, there can be lateral variations of these two minerals in the upper mantle. In the lower mantle, an increase of fp $(\text{Mg}, \text{Fe})\text{O}$ with respect to br $(\text{Mg}, \text{Fe})\text{SiO}_3$ would increase $(\text{Mg} + \text{Fe})/\text{Si}$ but decrease density because of the lower density of fp with respect to br (Ricolleau et al. 2009). V_S distributions resemble those of ρ , which suggests the same underlying causes (relative quantities of ol, px; br, fp) for their lateral variations. σ shows something like a mirror image; the higher conductivity of fp relative to br (Yoshino 2010) could lead to a positive correlation with $(\text{Mg} + \text{Fe})/\text{Si}$. However, it is not clear why there should be a negative correlation involving ol and px contents (Fig. 5.7i). None of the properties in this row resembles the T -effects of the first and second rows, and this argues for complex changes in mineralogy. Note that $(\text{Mg} + \text{Fe})/\text{Si}$ from 1 to 2 corresponds to a bulk composition from pyroxene to olivine stoichiometry, i.e., in the ranges of peridotites. The correlations of Fig. 5.7j reflect the tight linkages created by the forward operations g_2 and g_4 . The final column of Fig. 5.4 maps upper mantle mineral fractions $\text{px}/(\text{ol} + \text{px})$ and lower mantle $\text{fp}/(\text{br} + \text{fp})$. In both cases, the maps show good correlation between bulk chemistry and mineralogy. Because these minerals volumetrically dominate their respective depth ranges, they are of the most interest. Minor minerals are included in volumetric proportions for density and for elastic wave velocities in the VRH averaging scheme. However, because they are unlikely to form interconnected phases, their contributions to electrical conductivity are less significant and therefore more easily neglected.



◀ **Fig. 5.4** Maps of mean mantle thermochemical anomalies and variations in physical properties beneath Australia. Isotropic mantle shear-wave velocity (first column), electrical conductivity(second column), density (third column), temperature (fourth column), (Mg + Fe)/Si (fifth column, atomic fraction), Fe/(Fe + Mg) (sixth column, atomic fraction), and upper and lower mantle mineral ratios px/(ol + px) and fp/(br + fp) (seventh column, atomic fraction). Shear-wave speed, density, and temperature are given in % deviations from a mean model (Fig. 5.5), respectively. Electrical conductivity is relative to a reference electrical conductivity profile (Fig. 5.5). Mean reference values for all properties are indicated on the *right side* of each panel. Note that *color bars* are inverted for shear-wave speed and conductivity so that fast (slow) velocity anomalies correspond to low (high) conductivities

Figure 5.8 presents another picture in which thermochemical parameters are implicit, and it thus displays lateral interrelationships between physical properties. The overall picture behaves somewhat like the T -effects in the first row of Fig. 5.7; there is declining significance of T variation with depth. Relations in the first figure represent velocity–density systematics (e.g., Birch 1961; Shankland 1977). The most positive correlations characterize the case where density increases in different mineral phases having minimal change of chemical composition as represented by mean atomic weight \bar{m} . Mean atomic weight equals molecular weight of a compound divided by the number of atoms in its chemical formula and mostly reflects Fe enrichment. For instance, in the olivine series $((\text{Mg}_{1-x}, \text{Fe}_x)_2\text{SiO}_4)$ \bar{m} varies with x from 20.1 to 29.1. Negative correlations are strongest in a given crystal phase for increasing iron content. It appears that the wide range of lateral correlations in Fig. 5.8a could represent both effects beneath the Australian continent.

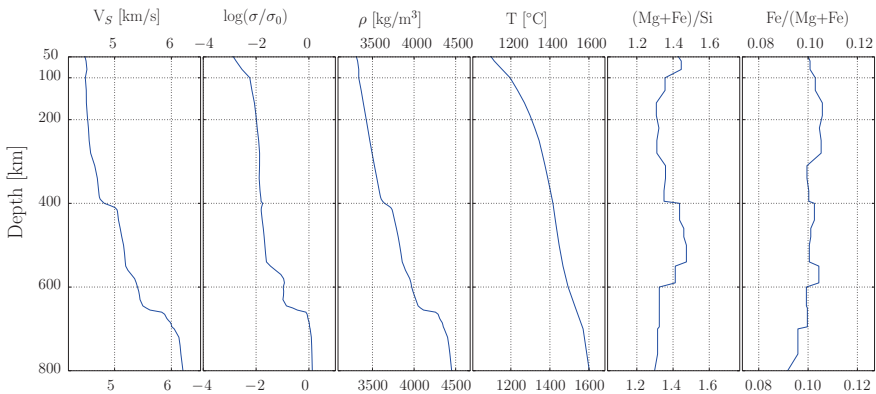


Fig. 5.5 Mean reference profiles (*blue*) showing radial variations in shear-wave speed (V_S), electrical conductivity $\log(\sigma/\sigma_0)$, density (ρ), temperature (T), and composition (Mg + Fe)/Si and Fe/(Mg + Fe) in atomic fractions, respectively. The mean profiles were constructed from lateral averages of each property at every depth node. In the conductivity plot $\sigma_0 = 1$ S/m

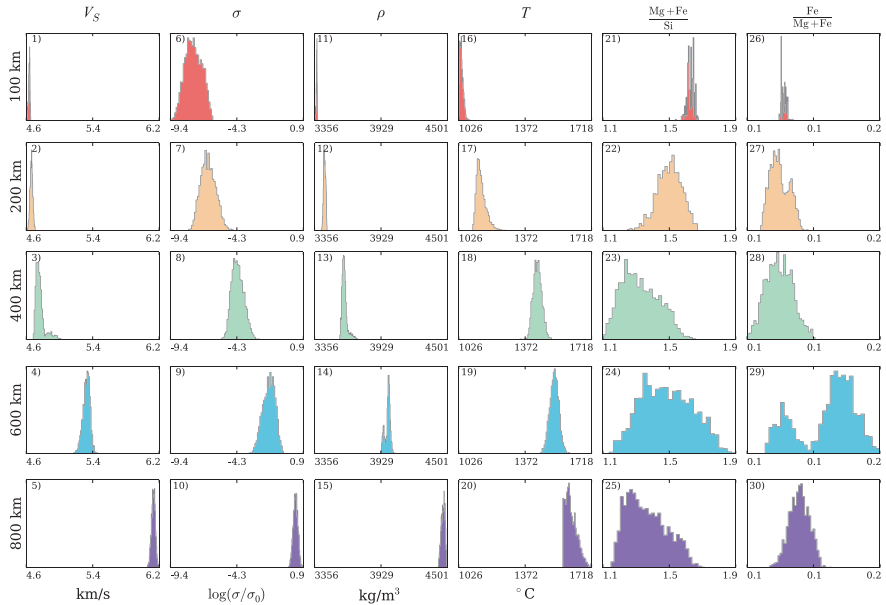


Fig. 5.6 One-dimensional marginal distributions for the model parameters are shown in Fig. 5.5 for a specific location in the center of the Australian continent (120°E, 27°S). Compositional distributions (Mg + Fe/Si and Fe/Mg + Fe) are in atomic fractions. In the conductivity plot $\sigma_0 = 1 \text{ S/m}$

5.3.2 Upper Mantle Structure

There is a good correlation in the upper mantle where shear-wave, density, and conductivity anomalies outline the continental boundaries of the region. Lateral velocity variations are commonly observed in seismic tomography images of the region (e.g., Fishwick and Rawlinson 2012; Kennett et al. 2012; Rawlinson et al. 2015). The continental regime has a distinct thermochemical signature and is divided into slow (corresponding to “hot” with relatively low (Mg + Fe)/Si and high Fe/(Mg + Fe) values) and fast (corresponding to “cold” with relatively high (Mg + Fe)/Si and low Fe/(Mg + Fe) values) patterns that extend well into the upper mantle.

Fe/(Mg + Fe) is of order 0.1 ± 0.03 in mantle minerals; higher ratios yield higher conductivities (e.g., Hirsch et al. 1993) principally in the polaron reaction $\text{Fe}^{2+} \rightleftharpoons \text{Fe}^{2+} + e^-$. Moreover, low upper mantle conductivities clearly correlate with fast velocity and positive density anomalies over the older western and central parts of the continent, whereas high conductivity anomalies correlate with slow velocity and negative density variations over the younger eastern and oceanic lithospheric regions. This conductivity pattern has not been resolved previously; to first order, it appears to be governed by temperature variations through the strong T -dependence of σ .

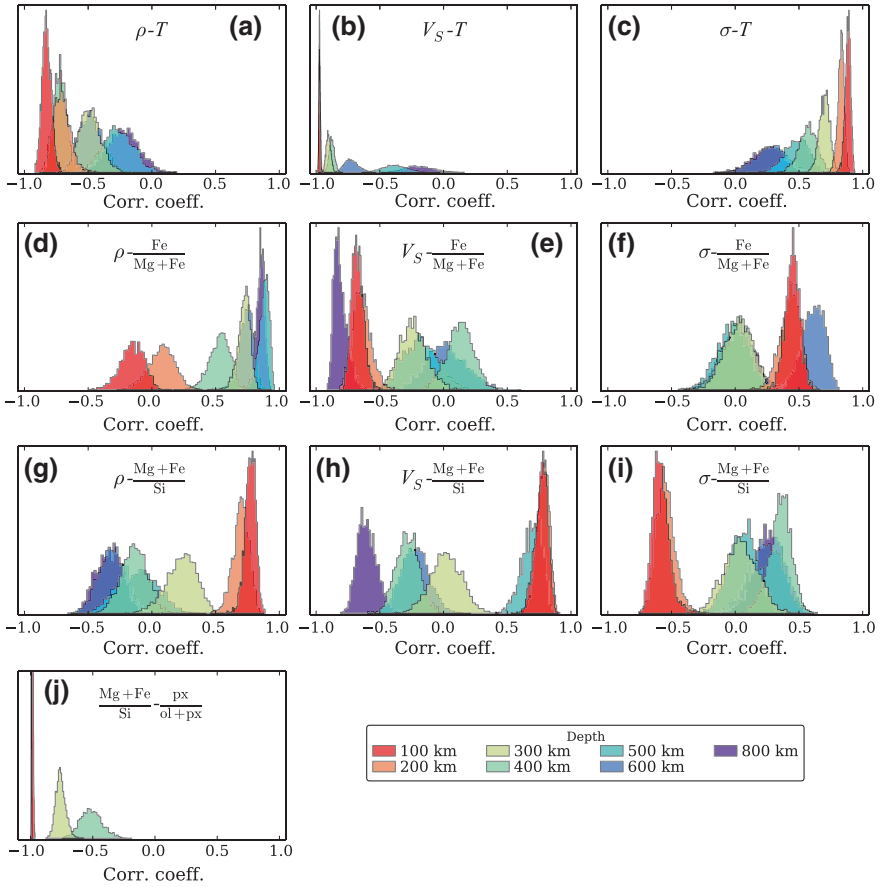


Fig. 5.7 Correlation between physical and thermochemical parameters as functions of depth. Distributions are normalized to unity for the highest peak in each plot, i.e., peak heights/widths are independent between the various properties shown (e.g., $V_S - T$ and $V_S - \text{Fe}/\text{Mg} + \text{Fe}$)

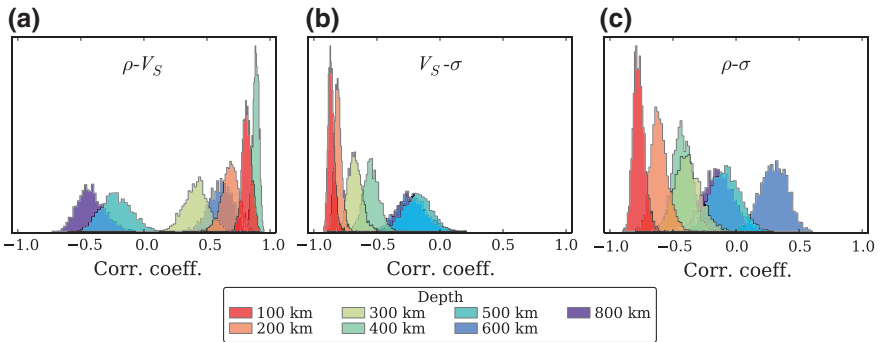


Fig. 5.8 Correlation between physical parameters as functions of depth. Distributions are normalized to unity for the highest peak, i.e., peak heights/widths are independent between the various properties shown (e.g., $V_S - T$ and $V_S - \text{Fe}/\text{Mg} + \text{Fe}$)

This observation is strongly supported by the distribution of correlation coefficients (Fig. 5.7). The correlation pairs $V_S - T$, $\rho - T$, and $\sigma - T$ are very peaked in the depth range 100–300 km relative to, e.g., $\text{Fe}/(\text{Mg} + \text{Fe})$ and $(\text{Mg} + \text{Fe})/\text{Si}$, although compositional variations do appear to be important. In particular, we observe ρ to correlate positively with $(\text{Mg} + \text{Fe})/\text{Si}$ and V_S and σ to correlate with both $\text{Fe}/(\text{Mg} + \text{Fe})$ and $(\text{Mg} + \text{Fe})/\text{Si}$. The absolute values of the correlation coefficients are as expected in the case of temperature, with negative correlations existing for $V_S - T$ and $\rho - T$ and positive correlations for $\sigma - T$.

Toward the bottom of the upper mantle, thermal effects become progressively less important, giving way to more complex compositionally-dependent structures. This is most apparent in the case of ρ at 300 km depth, which reveals a relatively strong compositional signature that correlates positively with $\text{Fe}/(\text{Mg} + \text{Fe})$. In contrast, V_S and σ are largely controlled by lateral thermal effects (Fig. 5.7b, c). For additional discussion of upper mantle structure see the contributions by Rawlinson et al. (2015), Schmerr (2015), and Katsura and Yoshino (2015).

5.3.3 Transition Zone and Lower Mantle Structure

Within the transition zone (400–600 km depth), lateral velocity, density, and conductivity variations are reflected in correlations between the various parameters. Temperature has less influence compared with chemical/mineral contributions. Lateral changes of ρ correlate strongly with $\text{Fe}/(\text{Mg} + \text{Fe})$ in particular, a result of substituting the heavier Fe atom for Mg. However, transition zone density correlates poorly with oxide (mineral) content, and V_S behaves similarly, which would argue for incoherent lateral variation in these properties. V - ρ systematics Fig. 5.8a has more structure with more lateral changes still in the range close to zero correlations. This also holds for electrical conductivity except for the 600 km regime. Here, the $\text{Fe}/(\text{Mg} + \text{Fe})$ -dependence at 600 km probably relates to conductivity dependence on Fe in transition-zone minerals, particularly in ringwoodite (Yoshino and Katsura 2013). The lower transition zone beneath the main continent appears to have a different style of lateral variation with slow velocity, negative density, and weak-to-positive conductivity relations. Overall, transition zone displays a general decoupling of structure relative to the upper mantle which is driven by an increase in $(\text{Mg} + \text{Fe})/\text{Si}$ with depth, (Fig. 5.5). The decoupling appears uncorrelated with $\text{Fe}/(\text{Mg} + \text{Fe})$, while thermal anomalies are smoothed out and less dominant relative to the upper mantle. For additional discussion of transition zone structure see the contribution by Kawai and Tsuchiya (2015).

In the outermost lower mantle (800 km depth), variations in all properties diminish in amplitude, in agreement with a lower mantle that is governed by small-amplitude thermochemical variations (e.g., Jackson 1998). Figure 5.7 reveals that both ρ and V_S correlate strongly with $\text{Fe}/(\text{Mg} + \text{Fe})$, although with opposite signs, resulting in a negative correlation between ρ and V_S in the outermost lower mantle. V_S also shows significant negative correlation with $(\text{Mg} + \text{Fe})/\text{Si}$.

Si. The weak negative correlation in Fig. 5.8a suggests lateral Fe enrichment in the lower mantle (in contrast to lateral mineralogical variation in the upper mantle). The small-scale features found here suggest a relatively homogeneous lower mantle. This observation is in line with what is inferred from global seismic tomography that also shows low-amplitude velocity variations in the lower mantle (e.g., Kustowski et al. 2008).

5.3.4 Comparison with Other Studies

The shear wave-speed variations found here in the upper mantle have, as discussed in more detail in Khan et al. (2013), also been reported elsewhere (see the Australian upper mantle seismic tomography models of, e.g., Fichtner et al. (2010), Fishwick and Rawlinson (2012), Kennett et al. (2012). Most of these models (not shown for brevity) are sensitive to about 300 km. Their prominent features to this depth include separation of structure into tectonic regimes that are slow (corresponding to our relatively “hot,” low Fe/(Mg + Fe) and (Mg + Fe)/Si) or fast (relatively “cold,” high Fe/(Mg + Fe) and (Mg + Fe)/Si). Details among the various models nonetheless differ as a result of differences in methodology, data, and parameterization. However, the overall level of agreement with other regional models is encouraging and is considered evidence in support of the joint thermodynamic analysis performed here.

Several studies have tried to unravel the physical causes of the observed velocity variations that are seen in seismic tomography images (e.g., Masters et al. 2000; Saltzer et al. 2001; Deschamps et al. 2002; Deschamps and Trampert 2003; Resovsky and Trampert 2003; Simmons et al. 2009; Afonso et al. 2010). For this purpose, the ratio of relative changes in shear (V_S) and compressional wave velocities (V_P), defined as $R_{P/S} = \partial \ln V_S / \partial \ln V_P$, has been computed directly from seismic P - and S -wave tomography models. An increase in $R_{P/S}$ with depth is thought to indicate an increased compositional contribution to the observed structural variations. Generally, these studies find that the mean value of $R_{P/S}$ increases radially, although important, but less-defined, lateral variations also exist. However, as is often the case independent overlapping information on P - and S -wave velocities is not available, and even in cases where it is, Deschamps and Trampert (2003) have shown that $R_{P/S}$ is only able to provide qualitative indication of chemical variations. Deschamps and Trampert (2003), nonetheless conclude from the distribution of $R_{P/S}$ and its dispersion that the cause of P - and S -wave speed anomalies is not only temperature, but it likely bears a compositional component. However, separation of thermal and chemical effects by seismic wave-speeds alone is difficult and, as already mentioned, is further complicated by the relative insensitivity of seismic wave-speeds to the density contrasts that must ultimately drive mantle convection.

This contrasts with the approach here where composition and temperature act as fundamental parameters, that, when connected to geophysical data via material

properties through self-consistent thermodynamic computations of mineral phase equilibria provides a natural means of determining all properties and their variations simultaneously. This obviates the need for unknown or *ad hoc* scaling relationships between the various physical parameters as typically invoked in seismic tomography. The advantage of our scheme is that geophysical/petrological knowledge is implicitly involved, so that more physically realistic models that depend only on the specific composition, temperature, and pressure conditions are produced. For example, electrical conductivity can enhance pictures of mineral composition and density in mantle models.

Limited comparisons for upper mantle conductivity models of the region are available. A conductivity-depth profile based on the Australian hemisphere model of solar quiet (S_q) daily variations was obtained by Campbell et al. (1998). Conductivities were found to range from 0.02 to 0.04 S/m at 200 km depth to 0.1–0.15 S/m at 400 km depth in general agreement with present findings. Comparison with the global 3D conductivity models of Kelbert et al. (2009) and Semenov and Kuvshinov (2012) (not shown for brevity) is difficult given the low lateral resolution of their models on continental scales. Their models, valid in the depth range 400–1600 km, generally differ from each other by one log-unit in conductivity and appear to have few features in common with this work, although a somewhat higher conductivity anomaly over eastern Australia relative to the rest of the continent is discernable in both studies. This anomaly has also been observed recently by Koyama et al. (2014). Conductivities across the continent range from ~ 0.1 to ~ 1 S/m in the transition zone and increase to 1–3.5 S/m below. Anomaly patterns aside, these conductivity ranges essentially bracket those found here where conductivities range from ~ 0.05 to 1 S/m in the transition zone and ~ 1 to 3 S/m in the outermost lower mantle. For comparison, conductivities computed from laboratory data assuming a “standard” mantle adiabat and a uniform mantle composed of “dry” pyrolite lies in the range 0.1–0.3 S/m. Comparison of our Australian conductivity model with the model of Semenov and Kuvshinov (2012) shows some agreement, particularly in the lower mantle where both models appear relatively uniform. In the depth range 700–800 km, our model and Semenov and Kuvshinov’s model suggest conductivities around 1–2 and 1–3 S/m, respectively, whereas the models of Kelbert et al. and Tarits and Mandaia (2010) have larger variations that range from ~ 0.5 to 5 S/m to ~ 0.1 to 10 S/m, respectively. Such large conductivity variations can be difficult to explain in the apparent absence of unusually strong thermochemical anomalies associated with water and/or melt (Yoshino and Katsura 2013).

5.4 Testing the Conductivity Model Against Observations

To test this Australian conductivity model, we computed magnetic fields of 24 h S_q variations using the S3D method described in Koch and Kuvshinov (2013) and compared these to observed magnetic fields acquired from an Australia-wide

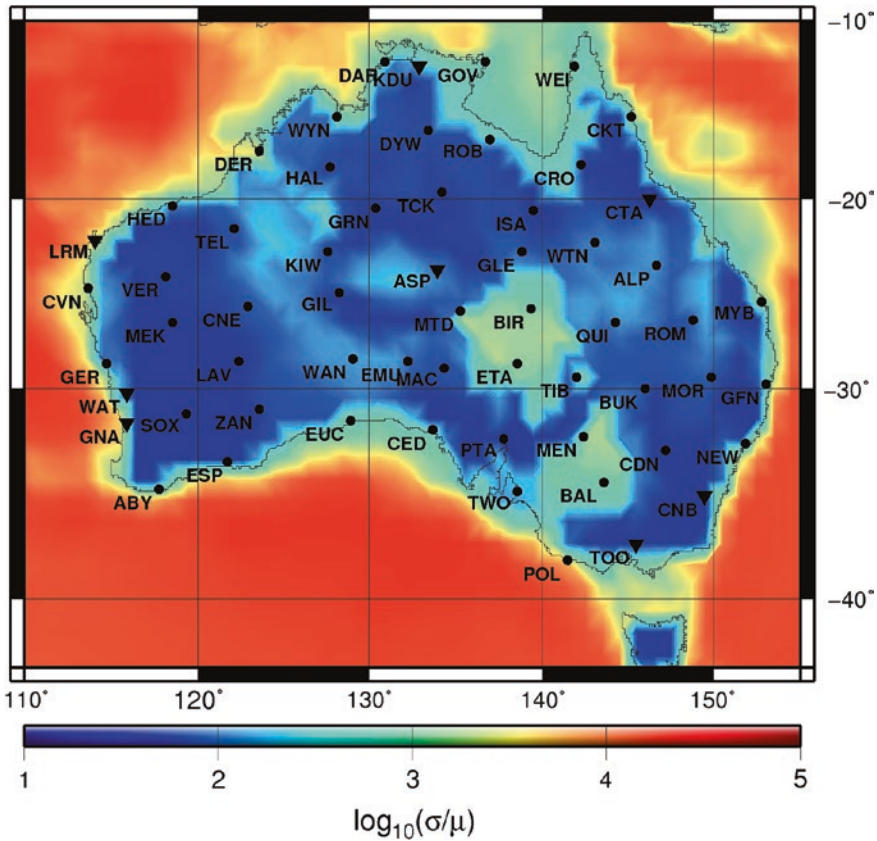


Fig. 5.9 Non-uniform surface conductance map (Manoj et al. 2006) used for magnetic field computations. Location of geomagnetic stations are also indicated: 53 non-permanent vector magnetometer (dots) of the Australia-wide array of geomagnetic stations (AWAGS) alongside with the eight permanent magnetic observatories (inverted triangles) of which four (CNB, CTA, GNA, and LRM) were part of AWAGS. $\mu = 1$ S

array of 57 3-component magnetometers (AWAGS) that operated for a period of 8 months (e.g., Chamalaun and Barton 1993). Station distribution and the currently employed surface conductance model are shown in Fig. 5.9. Observed and computed magnetic fields for all AWAGS stations based on our Australian model and a purely radial conductivity model (mean of the 3D model) are compared in Fig. 5.10. The misfit between models is computed from

$$B_{\text{mis}}(\theta, \phi) = \frac{1}{24} \sum_{i=1}^{24} B_i^{\text{obs}}(\theta, \phi) - B_i^{\text{mod}}(\theta, \phi), \tag{5.2}$$

where $B_i^{\text{obs}}(\theta, \phi)$ and $B_i^{\text{mod}}(\theta, \phi)$ represent observed and computed magnetic fields, respectively, at a given observatory.

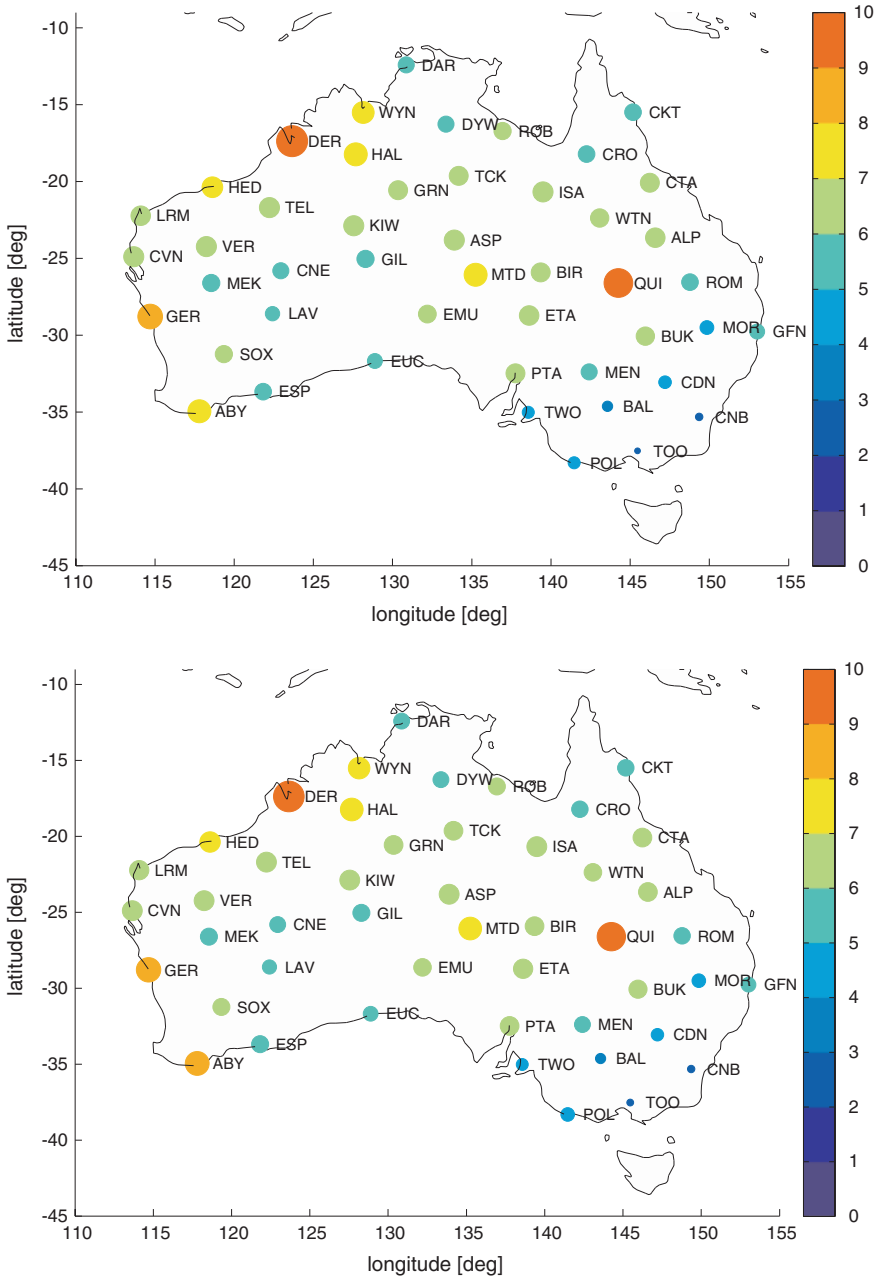


Fig. 5.10 Comparison between observed and computed horizontal magnetic fields across the Australia-wide array of geomagnetic stations (AWAGS) for the three-dimensional (3D) conductivity model is shown in Fig. 5.4 (a) and a radial one-dimensional conductivity model (mean of 3D model) (b). Both models are overlain by the non-uniform surface conductance map shown in Fig. 5.9. Color bar on the right side of each plot shows size of residual over 24 h as computed from Eq. 5.2 and is given in [nT]. Color coding as follows: *blue* (small) and *red* (big) circles designate small and large residuals, respectively

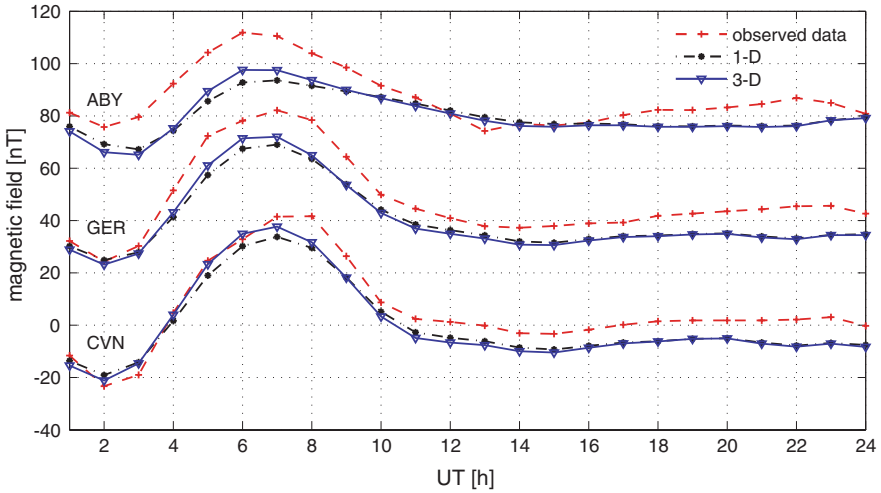


Fig. 5.11 Comparison of computed and observed horizontal-component magnetic fields of 24 h S_q -variations (May 15, 1990) at three representative observatories of the Australia-wide array of geomagnetic stations (AWAGS). *Dot-dashed curves* (labeled *1D*) designate synthetic data at observatory positions obtained using the surface conductance map shown in Fig. 5.9 and a one-dimensional (*1D*) conductivity background section constructed as the mean of the three-dimensional (*3D*) model. Solid curves (labeled *3D*) designate synthetic data at observatory positions obtained employing the same surface conductance shell map and the 3D upper mantle conductivity model (Fig. 5.4). Observed data are shown as *dashed lines*. In order to determine the S_q source that drives the forward modeling, we employed the S3D method (Koch and Kuvshinov 2013) for analysis of a magnetically very quiet day with the typical symmetric characteristic of the northern and southern S_q vortices

Examples of observed and computed magnetic field variations over a full 24 h-period at three stations are shown in Fig. 5.11; although misfits appear to be similar across the continent, differences between computed and observed magnetic fields are nonetheless observed to be present. The 3D conductivity model provides a better fit to data than the purely radial conductivity model (both overlain by the non-uniform surface conductance model shown in Fig. 5.9). The level of improvement relative to the purely radial model suggests that the lateral conductivity variations found here are supported by data, although further improvement in data fits probably calls for stronger regional variations than seen presently (e.g., Koyama et al. 2014). In this context, 3D global conductivity models (e.g., Kelbert et al. 2009; Tarits and Mandaia 2010; Semenov and Kuvshinov 2012) show anomalies that vary several orders of magnitude across regions spanning continents and oceans. This difference between field- and laboratory-derived conductivities has presented long-standing difficulties.

An explanation for the discrepancy between conductivities determined in the laboratory and those derived from long-period EM-induction data could be due to inadequate or incomplete modeling of the magnetospheric source. Thus, if a complex source is modeled using a simple source structure such as P_0^1 (implicit in the

C-response concept), for example, then a large part of the modeled signal could be regarded as emanating entirely from the mantle. Such an effect could potentially lead to overestimation of mantle conductivity. This hypothesis is currently being investigated by Püthe et al. (2015) who are studying the use and implications of a set of new transfer functions that account for complex source structures when inverting global EM-induction data. Indeed, Püthe et al. (2015) find that inaccurate description of source structure leads to erroneous estimations of mantle conductivity.

5.5 Conclusions

The connection between geophysical observables, physical rock properties (seismic wave-speeds, density, and electrical conductivity), and thermo-chemistry is contained in the use of a self-consistent thermodynamic modeling scheme of mantle mineral phase equilibria that depends only on composition, temperature, and pressure. The great advantage of this approach is that it inserts geophysical/petrological knowledge of, e.g., discontinuities that straightforward inversions would not necessarily be able to resolve even though they have to be present. In this manner, we produce profiles of physical properties to obtain models of mantle conditions that simultaneously combine features of both laboratory and geophysical data.

In this study, we have examined the relative behavior between various mantle physical properties (elasticity, density, and electrical conductivity) that derive from stochastic inversion of seismic data. We have presented maps of the three-dimensional density, electrical conductivity, and shear-wave speed of the mantle beneath Australia and surrounding ocean in the depth range 100–800 km. The inversion mapped mantle temperatures and compositions, which, when combined with independent laboratory conductivity measurements of different mineralogies and temperatures, allowed us to compute mantle electrical conductivities at depth. Thus, although the conductivity maps obtained here are not constrained by data that are directly sensitive to conductivity (e.g., electromagnetic sounding data or magnetic data), we have calculated equivalent magnetic response data for a model and compared these to observations.

For Australia and its surroundings, we have shown from a combined analysis of seismic surface-wave data, phase-equilibrium computations, and laboratory-measured electrical conductivities that in the upper mantle seismic wave-speed, density, and conductivity anomalies appear to follow continental boundaries. Low conductivities correlate with the old stable central and western parts of the continent (relatively cold and seismically fast and dense), whereas high conductivity anomalies correlate with younger continental regions and oceanic lithosphere (relatively hot and seismically slow and less dense). Contributions to variations in structure are to a large extent temperature-controlled, although composition does appear to play a non-negligible role. Toward the bottom of the upper mantle and within the transition-zone lateral shear-wave speed, density, and conductivity variations appear

to correlate less in comparison with the upper mantle, which suggests a compositional signature in observed anomaly patterns. Apart from the strong changes in properties that occur at seismic discontinuities, which are due to variations in thermochemically induced phase transformation of olivine to wadsleyite, transition-zone shear-wave speed, density, and conductivity maps are relatively smooth—a distinct feature of many seismic tomography images. In the lower mantle, compositional variations seem to govern relative behaviors of shear-wave speeds and conductivity to a greater extent than in the shallower mantle. There is additional evidence for bulk compositional variations between upper and lower mantle with the transition zone possibly acting as an intermediary layer.

Finally, the 3D regional conductivity model presented here has been tested against observed magnetic fields based on S_q -variations from an Australia-wide array of geomagnetic stations and found to provide an adequate fit. As a result, the present model should be a good choice as a starting model for 3D electromagnetic inversions of the Australian region. Validation of the proposed conductivity model will have to await solution of the inverse problem, which will be the focus of future studies.

Acknowledgements We wish to thank J.C. Afonso and an anonymous reviewer for helpful comments as well as T. Koyama, C. Püthe, and A. Kuvshinov for informed discussions. TJS thanks the Office of Basic Energy Sciences, U.S. Department of Energy for support. Numerical computations were performed on the ETH cluster Brutus.

References

- Afonso JC, Ranalli G, Fernandez M, Griffin WL, O'Reilly SY, Faul U (2010) On the V_p/V_s —Mg# correlation in mantle peridotites: implications for the identification of thermal and compositional anomalies in the upper mantle. *Earth Planet Sci Lett* 289:606
- Afonso JC, Fullea J, Griffin WL, Yang Y, Jones AG, Connolly JAD, O'Reilly SY (2013a) 3D multi-observable probabilistic inversion for the compositional and thermal structure of the lithosphere and upper mantle I: a priori information and geophysical observables. *J Geophys Res.* doi:[10.1002/jgrb.50124](https://doi.org/10.1002/jgrb.50124)
- Afonso JC, Fullea J, Yang Y, Connolly JAD, Jones AG (2013b) 3D multi-observable probabilistic inversion for the compositional and thermal structure of the lithosphere and upper mantle II: general methodology and resolution analysis. *J Geophys Res.* doi:[10.1002/jgrb.50123](https://doi.org/10.1002/jgrb.50123)
- Berryman JG (1995) Mixture theories for rock properties. In: Ahrens TJ (ed) *American geophysical union handbook of physical constants*. AGU, New York, p 205
- Bina CR (1998) Free energy minimization by simulated annealing with applications to lithospheric slabs and mantle plumes. *Pure Appl Geophys* 151:605
- Birch F (1961) The velocity of compressional waves in rocks to 10 kilobars, 2. *J Geophys Res* 66:2199
- Brown JM, Shankland TJ (1981) Thermodynamic parameters in the earth as determined from seismic profiles. *Geophys J Int* 66:579
- Campbell WH, Barton CE, Chamalaun FH, Webb W (1998) Quiet-day ionospheric currents and their applications to upper mantle conductivity in Australia. *Earth Planet Space* 50:347
- Chamalaun FH, Barton CE (1993) Electromagnetic induction in the Australian crust: results from the Australia-wide array of geomagnetic stations. *Explor Geophys* 24:179

- Christensen UR, Hofmann AW (1994) Segregation of subducted oceanic crust in the convecting mantle. *J Geophys Res* 99(19):867. doi:[10.1029/93JB03403](https://doi.org/10.1029/93JB03403)
- Connolly JAD (2005) Computation of phase equilibria by linear programming: a tool for geodynamic modeling and an application to subduction zone decarbonation. *Earth Planet Sci Lett* 236, doi:[10.1016/j.epsl.2005.04.033](https://doi.org/10.1016/j.epsl.2005.04.033)
- Connolly JAD (2009) The geodynamic equation of state: what and how. *Geophys Geochem Geosys* 10:Q10014. doi:[10.1029/2009GC002540](https://doi.org/10.1029/2009GC002540)
- Deschamps F, Trampert J (2003) Mantle tomography and its relation to temperature and composition. *Phys Earth Planet Int* 140:277
- Deschamps F, Snieder R, Trampert J (2001) The relative density-to-shear velocity scaling in the uppermost mantle. *Phys Earth Planet Int* 124:193
- Deschamps F, Trampert J, Snieder R (2002) Anomalies of temperature and iron in the uppermost mantle inferred from gravity data and tomographic models. *Phys Earth Planet Int* 129:245
- Dobson DP, Brodholt JP (2000) The electrical conductivity and thermal profile of the Earth's mid-mantle. *Geophys Res Lett* 27:2325
- Drilleau M, Beucler E, Mocquet A, Verhoeven O, Moebs G, Burgos G, Montagner J-P, Vacher P (2013) A Bayesian approach to infer radial models of temperature and anisotropy in the transition zone from surface wave data. *Geophys J Int.* doi:[10.1093/gji/ggt284](https://doi.org/10.1093/gji/ggt284)
- Fabricnaya OB (1999) The phase in the FeO–MgO–Al₂O₃–SiO₂ system: assessment of thermodynamic properties and phase equilibria at pressures up to 30 GPa. *Calphad* 23:19
- Fichtner A, Kennett BLN, Igel H, Bunge H-P (2010) Full waveform tomography for radially anisotropic structure: new insights into present and past states of the Australasian upper mantle. *Earth Planet Sci Lett* 290, doi:[10.1016/j.epsl.2009.12.003](https://doi.org/10.1016/j.epsl.2009.12.003)
- Fishwick S, Rawlinson N (2012) 3-D structure of the Australian lithosphere from evolving seismic datasets. *Austr J Earth Sci* 59:809
- Forte AM, Perry HC (2000) Geodynamic evidence for a chemically depleted continental tectosphere. *Science* 290:1940
- Fullea J, Afonso JC, Connolly JAD, Fernandez M, Garcia-Castellanos D, Zeyen H (2009) LitMod3D: an interactive 3D software to model the thermal, compositional, density, rheological, and seismological structure of the lithosphere and sublithospheric upper mantle. *Geochem Geophys Geosyst* 10:Q08019. doi:[10.1029/2009GC002391](https://doi.org/10.1029/2009GC002391)
- Fullea J, Muller MR, Jones AG (2011) Electrical conductivity of continental lithospheric mantle from integrated geophysical and petrological modeling: application to the Kaapvaal Craton and Rehoboth Terrane, southern Africa. *J Geophys Res* 116:B10202. doi:[10.1029/2011JB008544](https://doi.org/10.1029/2011JB008544)
- Fullea J, Lebedev S, Agius MR, Jones AG, Afonso JC (2012) Lithospheric structure in the Baikal central Mongolia region from integrated geophysical-petrological inversion of surface-wave data and topographic elevation. *Geochem Geophys Geosyst* 13, Q0AK09. doi:[10.1029/2012GC004138](https://doi.org/10.1029/2012GC004138)
- Goes S, Govers R, Vacher P (2000) Shallow mantle temperatures under Europe from P and S wave tomography. *J Geophys Res* 105:11153
- Goes S, Armitage J, Harmon N, Smith H, Huismans R et al (2012) Low seismic velocities below mid-ocean ridges: attenuation versus melt retention. *J Geophys Res* 117. doi:[10.1029/2012JB009637](https://doi.org/10.1029/2012JB009637)
- Hashin Z, Shtrikman S (1962) A variational approach to the theory of effective magnetic permeability of multiphase materials. *J Appl Phys* 33:3125
- Helffrich GR, Wood BJ (2001) The Earth's Mantle. *Nature* 412–501
- Hirsch LM, Shankland TJ, Duba AG (1993) Electrical conduction and polaron mobility in Fe-bearing olivine. *Geophys J Int* 114:36
- Irfune T (1994) Absence of an aluminous phase in the upper part of the Earth's lower mantle. *Nature* 370:131
- Ishii M, Tromp J (2004) Constraining large-scale mantle heterogeneity using mantle and inner-core sensitive normal modes. *Phys Earth Planet Inter* 146:113

- Jackson I (1998) Elasticity, composition and temperature of the Earth's lower mantle: a reappraisal. *Geophys J Int* 134:291
- Jones AG, Afonso JC, Fulla J, Salajegheh F (2013) The lithosphere-asthenosphere system beneath Ireland from integrated geophysical-petrological modeling—I: observations, 1D and 2D hypothesis testing and modeling. *Lithos* (in press)
- Karato S-I (2011) Water distribution across the mantle transition zone and its implications for global material circulation. *Earth Planet Sci Lett* 301. doi:[10.1016/j.epsl.2010.1.038](https://doi.org/10.1016/j.epsl.2010.1.038)
- Katsura T, Yoshino T (2015) Heterogeneity of electrical conductivity in the oceanic upper mantle, this volume
- Kawai K, Tsuchiya T (2015) Elasticity of continental crust around the mantle transition zone, this volume
- Kelbert A, Schultz A, Egbert G (2009) Global electromagnetic induction constraints on transition-zone water content variations. *Nature* 460. doi:[10.1038/nature08257](https://doi.org/10.1038/nature08257)
- Kennett BLN (1998) On the density distribution within the Earth. *Geophys J Int* 132:374
- Kennett BLN, Fichtner A, Fishwick S, Yoshizawa K (2012) Australian seismological reference model (AuSREM): Mantle component. *Geophys J Int* 192. doi:[10.1093/gji/ggs065](https://doi.org/10.1093/gji/ggs065)
- Khan A, Shankland TJ (2012) A geophysical perspective on mantle water content and melting: inverting electromagnetic sounding data using laboratory-based electrical conductivity profiles. *Earth Planet Sci Lett* 317–318. doi:[10.1016/j.epsl.2011.11.031](https://doi.org/10.1016/j.epsl.2011.11.031)
- Khan A, Connolly JAD, Olsen N (2006) Constraining the composition and thermal state of the mantle beneath Europe from inversion of long-period electromagnetic sounding data. *J Geophys Res* 111:B10102. doi:[10.1029/2006JB004270](https://doi.org/10.1029/2006JB004270)
- Khan A, Kuvshinov A, Semenov A (2011) On the heterogeneous electrical conductivity structure of the Earth's mantle with implications for transition zone water content. *J Geophys Res* 116(B01103):2011. doi:[10.1029/2010JB007458](https://doi.org/10.1029/2010JB007458)
- Khan A, Zunino A, Deschamps F (2013) Upper mantle compositional variations and discontinuity topography imaged beneath Australia from Bayesian inversion of surface-wave phase velocities and thermochemical modeling. *J Geophys Res* 118. doi:[10.1002/jgrb.50304](https://doi.org/10.1002/jgrb.50304)
- Koch S, Kuvshinov A (2013) Global 3-D EM inversion of Sq-variations based on simultaneous source and conductivity determination. A concept validation and resolution studies. *Geophys J Int* doi:[10.1093/gji/ggt227](https://doi.org/10.1093/gji/ggt227)
- Koyama T, Shimizu H, Utada H, Ichiki M, Ohtani E, Hae R (2006) Water content in the mantle transition zone beneath the North Pacific derived from the electrical conductivity anomaly. In: Jacobsen S, van der Lee S (eds) *Earth's deep water cycle*, vol 168. AGU, Washington, DC, p 171 (*Geophys Monogr Ser*)
- Koyama T, Khan A, Kuvshinov A (2014) Three-dimensional electrical conductivity structure beneath Australia from inversion of geomagnetic observatory data: evidence for lateral variations in transition-zone temperature, water content, and melt. *Geophys J Int*. doi:[10.1093/gji/ggt455](https://doi.org/10.1093/gji/ggt455)
- Kuo C, Romanowicz B (2002) On the resolution of density anomalies in the Earth's mantle using spectral fitting of normal mode data. *Geophys J Int* 150:162
- Kuskov OL, Panferov AB (1991) Phase diagrams of the FeO–MgO–SiO₂ system and the structure of the mantle discontinuities. *Phys Chem Minerals* 17:642
- Kuskov OL, Kronrod VA, Prokofyev AA, Pavlenkova NI (2014) Thermo-chemical structure of the lithospheric mantle underneath the Siberian craton inferred from long-range seismic profiles. *Tectonophysics* 615616:154. doi:[10.1016/j.tecto.2014.01.006](https://doi.org/10.1016/j.tecto.2014.01.006)
- Kustowski B, Ekström G, Dziewonski AM (2008) Anisotropic shear-wave velocity structure of the Earth's mantle: a global model. *J Geophys Res* 113:B06306. doi:[10.1029/2007JB005169](https://doi.org/10.1029/2007JB005169)
- Kuvshinov A (2012) Deep electromagnetic studies from land, sea and space. Progress status in the past 10 years. *Surv Geophys* 33. doi:[10.1007/s10712-011-9118-2](https://doi.org/10.1007/s10712-011-9118-2)
- Landauer R (1952) The electrical resistance of binary metallic mixtures. *J Appl Phys* 23:779
- Laske G, Markee A, Orcutt JA, Wolfe CJ, Collins JA, Solomon SC, Detrick RS, Bercovici D, Hauri EH (2011) Asymmetric shallow mantle structure beneath the Hawaiian Swell—evidence from Rayleigh waves recorded by the PLUME network. *Geophys J Int* 187(1725):2011

- Lekic V, Romanowicz B (2012) Tectonic regionalization without a priori information: a cluster analysis of upper mantle tomography. *Earth Planet. Sci Lett* 308, doi:[10.1016/j.epsl.2011.05.050](https://doi.org/10.1016/j.epsl.2011.05.050)
- Manoj C, Kuvshinov A, Maus S, Lühr H (2006) Ocean circulation generated magnetic signals. *Earth Planet Space* 58:429
- Manthilake M, Matsuzaki T, Yoshino T, Yamashita S, Ito E, Katsura T (2009) Electrical conductivity of wadsleyite as a function of temperature and water content. *Phys Earth Planet Int.* doi:[10.1016/j.pepi.2008.06.001](https://doi.org/10.1016/j.pepi.2008.06.001)
- Masters G, Laske G, Bolton H, Dziewonski AM (2000) The relative behaviour of shear velocity, bulk sound speed, and compressional velocity in the mantle: Implications for chemical and thermal structure. In: Karato et al. (eds) *Earths deep interior: mineral physics and tomography from the atlantic to the global scale*, vol 117. AGU, Washington, DC, p 63 (Geophys Monogr Ser)
- Park SK, Ducea MN (2003) Can in situ measurements of mantle electrical conductivity be used to infer properties of partial melts? *J Geophys Res* 108:2270. doi:[10.1029/2002JB001899](https://doi.org/10.1029/2002JB001899)
- Piazzoni AS, Steinle-Neumann G, Bunge HP, Dolejs D (2007) A mineralogical model for density and elasticity of the Earth's mantle. *Geochem Geophys Geosyst* 8:Q11010. doi:[10.1029/2007GC001697](https://doi.org/10.1029/2007GC001697)
- Poirier JP (2000) *Introduction to the physics of the Earth's interior*, 2nd edn. Cambridge University Press, Cambridge, p 312
- Pommier A (2014) Interpretation of magnetotelluric results using laboratory measurements. *Surv Geophys* 35. doi:[10.1007/s10712-013-9226-2](https://doi.org/10.1007/s10712-013-9226-2)
- Püthe C, Kuvshinov A, Olsen N (2015) Handling complex source structures in global EM induction studies: from C-responses to new arrays of transfer functions. *Geophys J Int* 201, doi:[10.1093/gji/ggv021](https://doi.org/10.1093/gji/ggv021)
- Rawlinson N, Kennett BLN, Salmon M, Glen RA (2015) Origin of lateral heterogeneities in the upper mantle beneath south-east australia from seismic tomography, this volume
- Resovsky JS, Ritzwoller MH (1999) Regularization uncertainty in density models estimated from normal mode data. *Geophys Res Lett* 26:2319
- Resovsky J, Trampert J (2003) Using probabilistic seismic tomography to test mantle velocity-density relationships. *Earth Planet Sci Lett* 215:121
- Ricard Y, Mattern E, Matas J (2005) Synthetic tomographic images of slabs from mineral physics. In: Hilst RVD, Bass JD, Matas J, Trampert J (eds) *Earths deep Mantle: structure, composition, and evolution*. AGU, Washington, DC, pp 283–300
- Ricolleau et al (2009) Density profile of pyrolite under the lower mantle conditions. *Geophys Res Lett* 36:L06302. doi:[10.1029/2008GL036759](https://doi.org/10.1029/2008GL036759)
- Romanowicz B (2001) Can we resolve 3D density heterogeneity in the lower mantle? *Geophys Res Lett* 28:1107
- Saltzer RL, van der Hilst RH, Karason H (2001) Comparing P and S wave heterogeneity in the mantle. *Geophys Res Lett* 28:1335
- Saxena SK, Eriksson G (1983) Theoretical computation of mineral assemblages in pyrolite and lherzolite. *J Petrol* 24:538
- Schaeffer AJ, Lebedev S (2015) Global heterogeneity of the lithosphere and underlying mantle: a seismological appraisal based on multimode surface-wave dispersion analysis, shear-velocity tomography, and tectonic regionalization, this volume
- Schmerr N (2015) Imaging mantle heterogeneity with upper mantle seismic discontinuities, this volume
- Semenov A, Kuvshinov A (2012) Global 3-D imaging of mantle electrical conductivity based on inversion of observatory C-responses—II. Data analysis and results. *Geophys. J Int.* doi:[10.1111/j.1365-246X.2012.05665.x](https://doi.org/10.1111/j.1365-246X.2012.05665.x)
- Shankland TJ (1972) Velocity-density systematics: derivation from Debye theory and the effect of ionic size. *J Geophys Res* 77:3750
- Shankland TJ (1977) Elastic properties, chemical composition, and crystal structure of minerals. *Surv Geophys* 3:89

- Shankland TJ (1981) Electrical conduction in Mantle materials. In: O'Connell RJ, Fyfe WS (eds) *Evolution of the Earth*, American Geophysical Union, vol 5. Washington, DC. p 256, doi:[10.1029/GD005p0256](https://doi.org/10.1029/GD005p0256)
- Shankland TJ, O'Connell RJ, Waff HS (1981) Geophysical constraints on partial melt in the upper mantle. *Rev Geophys Space Phys* 19:394
- Shimizu H, Utada H, Baba K, Koyama T, Obayashi M, Fuka Y (2010) Three-dimensional imaging of electrical conductivity in the mantle transition zone beneath the North Pacific Ocean by a semi-global induction study. *Phys Earth Planet Int* 183. doi:[10.1016/j.pepi.2010.01.010](https://doi.org/10.1016/j.pepi.2010.01.010)
- Simmons NA, Forte AM, Grand SP (2009) Joint seismic, geodynamic and mineral physical constraints on three-dimensional mantle heterogeneity: Implications for the relative importance of thermal versus compositional heterogeneity. *Geophys J Int* 177:1284
- Sobolev SV, Babeyko AY (1994) Modeling of mineralogical composition, density and elastic-wave velocities in anhydrous magmatic rocks. *Surv Geophys* 15:515
- Stixrude L, Lithgow-Bertelloni C (2005) Thermodynamics of mantle minerals I. Physical properties. *Geophys J Int* 162:610
- Stixrude L, Lithgow-Bertelloni C (2011) Thermodynamics of mantle minerals II. Phase equilibria. *Geophys J Int* 184:1180
- Tarits P, Manda M (2010) The heterogeneous electrical conductivity structure of the lower mantle. *Phys Earth Planet Int* 183. doi:[10.1016/j.pepi.2010.08.002](https://doi.org/10.1016/j.pepi.2010.08.002)
- Toffelmier DA, Tyburczy JA (2007) Electromagnetic detection of a 410-km-deep melt layer in the Southwestern United States. *Nature* 447. doi:[10.1038/nature05922](https://doi.org/10.1038/nature05922)
- Trampert J, Van der Hilst RD (2005) Towards a quantitative interpretation of global seismic tomography. In: Van der Hilst RD, Bass JD, Matas J, Trampert J (eds) *Earth's Deep Interior: Structure, Composition, and Evolution*, Geophysical Monograph 160. American Geophysical Union, Washington, p 47–62
- Utada, H., Koyama, T., Obayashi, M., Fukao, Y., 2009. A joint interpretation of electromagnetic and seismic tomography models suggests the mantle transition zone below Europe is dry. *Earth Planet Sci Lett*. doi:[10.1016/j.epsl.2009.02.027](https://doi.org/10.1016/j.epsl.2009.02.027)
- Verhoeven O et al (2009) Constraints on thermal state and composition of the Earth's lower mantle from electromagnetic impedances and seismic data. *J Geophys Res* 114:B03302. doi:[10.1029/2008JB005678](https://doi.org/10.1029/2008JB005678)
- Wang CY (1970) Density and constitution of the mantle. *J Geophys Res* 75:3264
- Watt JP, Davies GF, O'Connell RJ (1976) The elastic properties of composite materials. *Rev Geophys Space Phys* 14:541
- Wood BJ, Holloway JR (1984) A thermodynamic model for subsolidus equilibria in the system CaO–MgO–Al₂O₃–SiO₂. *Geochim Cosmochim Acta* 66:159
- Xie S, Tackley PJ (2004) Evolution of helium and argon isotopes in a convecting mantle. *Phys Earth Planet Inter* 146:417. doi:[10.1016/j.pepi.2004.04.003](https://doi.org/10.1016/j.pepi.2004.04.003)
- Xu Y, Shankland TJ, Poe BT (2000) Laboratory-based electrical conductivity in the Earth's mantle. *J Geophys Res* 108:2314
- Yoshino T (2010) Laboratory electrical conductivity measurement of mantle minerals. *Surv Geophys* 31:163206. doi:[10.1007/s10712-009-9084-0](https://doi.org/10.1007/s10712-009-9084-0)
- Yoshino T, Katsura T (2013) Electrical conductivity of mantle minerals: role of water in conductivity anomalies. *Ann Rev Earth Planet Sci* 41. doi:[10.1146/annurev-earth-050212-124022](https://doi.org/10.1146/annurev-earth-050212-124022)
- Yoshino T et al (2012) Effect of temperature, pressure and iron content on the electrical conductivity of olivine and its high-pressure polymorphs. *J Geophys Res* 117:B08205. doi:[10.1029/2011JB008774](https://doi.org/10.1029/2011JB008774)